




# Experimental Characterization and Numerical Modelling of the Impact Behavior of PVC Foams

M. Sasso<sup>1</sup> · F. Sarasini<sup>2</sup> · E. Mancini<sup>3</sup> · A. Lattanzi<sup>1</sup>  · J. Tirillò<sup>2</sup> · C. Sergi<sup>2</sup>

Received: 27 September 2022 / Accepted: 28 February 2023  
© The Author(s) 2023

## Abstract

**Background** Polyvinyl chloride (PVC) foams are widely used in crashworthiness and energy absorption applications due to their low density and the capability of crushing up to large deformations with limited loads. This property is due to their particular constitutive behavior: the stress-strain curve is characterized, after an initial yield or peak stress, by a relevant plateau region followed by a steep increase due to foam densification. Furthermore, the mechanical response of PVC foam is strongly strain rate dependent.

**Objective** This work aims to characterize the mechanical behavior of PVC foams and to develop a complete constitutive model for impact and energy absorption applications.

**Methods** Compressive tests are carried out at different speeds on PVC foam samples having different relative densities. Quasi-static and intermediate strain rate tests are performed by a pneumatic machine, while high strain rate tests are conducted by means of a Split Hopkinson Pressure Bar. The uniaxial stress-strain curves are used to calibrate the visco-elastic and visco-plastic constitutive model. In particular, the material behavior is divided into two parallel branches: the former describes the elasto-plastic behavior, while the latter accounts for the visco-elastic one; the plastic branch also includes a multiplicative term accounting for the strain rate sensitivity of the base material.

**Results** The tests highlight a strong compressibility of the foam with negligible lateral expansion. The energy absorption efficiency, as well as the densification strain, is evaluated. The material model is also implemented in Finite Element (FE) simulations of puncture impact tests, validating the results of the calibration procedure.

**Conclusions** The calibration of the visco-elasto-plastic material model offers a physically consistent identification of the constitutive response of the PVC foams, showing an effective characterization of the impact behavior of the material.

**Keywords** PVC · Foam · Visco-elasticity · Visco-plasticity · Hopkinson bar

## Introduction

Polyvinyl chloride (PVC) is one of the so-called “commodity polymers” because of its low cost and availability in different grades, including high-elasticity blends. In the form

of foam, PVC is extensively employed in crashworthiness and energy absorption applications and in all those fields where impact or shock loadings must be attenuated. For instance, PVC foams are widely used as the core in sandwich panels [1, 2], in marine and underwater systems [3, 4],

✉ A. Lattanzi  
a.lattanzi@staff.univpm.it

M. Sasso  
m.sasso@staff.univpm.it

F. Sarasini  
fabrizio.sarasini@uniroma1.it

E. Mancini  
edoardo.mancini@univaq.it

J. Tirillò  
jacopo.tirillo@uniroma1.it

C. Sergi  
claudia.sergi@uniroma1.it

<sup>1</sup> Department of Industrial Engineering and Mathematical Sciences, Università Politecnica delle Marche, via Brecce Bianche 12, 60131 Ancona, Italy

<sup>2</sup> Department of Chemical Engineering Materials Environment, Sapienza-Università di Roma & UdR INSTM, Via Eudossiana 18, 00184 Roma, Italy

<sup>3</sup> Department of Industrial and Information Engineering and Economics (DIIIE), Università degli Studi dell'Aquila, Piazzale Ernesto Pontieri, 67100 L'Aquila, Italy

in civil structures [5], and in several sports equipment [6]. Their feasibility as performant core materials encouraged the investigation of different aspects of the sandwich structures achievable with them such as their bending behavior [7, 8], fatigue resistance [9] and impact response [2, 10].

The broad diffusion of PVC foams in energy absorption applications is certainly due to their low density combined with the capability of crushing up to large deformations with limited loads. In particular, the stress-strain curve is characterized by a plateau region after the yielding stress, followed by a steep increase in material stiffness due to foam densification [11]. After the initial linear elastic behavior regulated by foam cell walls bending, the wide plateau region – responsible for their energy absorbing capability – can be ascribed to the collapse mechanism of the cells, generally associated with brittle crushing, elastic buckling or plastic yielding of the material, triggered at almost constant loading conditions. When opposite cell walls start to experience mutual contact, the densification region is approached, and a strain hardening is observed.

Considering the second main application of PVC foams and the paramount importance of working with a core material characterized by high out-of-plane stiffness and strength, the compressive behavior of PVC foams was extensively studied in both quasi-static [12, 13] and dynamic [14–21] conditions. Despite the extensive experimental data available in the literature, an effective constitutive modelling of the material behavior is essential to make reliable predictions of the response of real objects by means of either analytical methods or finite element simulations. Over the years, several constitutive models have been developed to describe the stress-strain relationship of PVC and other polymeric foams. With regard to the elasto-plastic behavior, the modelling started from the seminal work by Rusch [22] and has been further developed in more complex analytical formulations by Gibson and Ashby [23], Liu and Subhash [24], and Avalle et al. [25], to describe the crushing behavior under large deformations. The evolution of damage has also been considered by Gielen [26].

Furthermore, the mechanical response of PVC foam is strongly influenced by the strain rate due to its viscoelastic nature. As most of the applications are related to dynamic or impact loading of the foams, proper characterization and modelling of their time-dependent behavior are fundamental. To account for this, different models have been proposed, in which the material strength is typically multiplied by an analytical function that incorporates strain rate [27, 28], and often temperature and density [29, 30]. As a result, the global behavior of a PVC foam can be described as the sum of various contributions, including elasto-plastic deformation and viscous effects.

In this framework, the present manuscript represents a step forward towards understanding the behavior of PVC foams

under compression loading, by addressing the effect of material density and strain rate. In particular, three different densities and four different test speeds – from quasi-static, to intermediate and high strain-rate regimes – are considered. The obtained stress-strain curves have been used to compute the energy absorption efficiency and the densification strain, according to the procedure described in [31, 32]. Finally, the uniaxial stress-strain curves are used to calibrate an innovative combined visco-elastic and visco-plastic constitutive model, based on a 2-layer scheme [33]. In the model, the material behavior is divided into two parallel branches: the first one represents the visco-elastic behavior, whereas the second one represents the visco-plastic behavior. In the latter, a multiplicative term is introduced to account for the strain rate sensitivity of the base material.

The analytical model is implemented in the commercial finite element (FE) software Abaqus<sup>®</sup>/Explicit through a VUMAT subroutine for the simulation of the puncture impact behavior of the foams under study. Also in this case, the analytical model proved to be an efficient tool to simulate material dynamic response providing a good fitting of the experimental curves in terms of both maximum indentation depth and punch speed profile. This proves the effectiveness of the proposed model even in working conditions that are well far from the pure compression employed to validate the analytical model.

## Tested Materials and Equipment

### Materials

In this work, parallelepiped samples of closed-cell PVC foam were tested to characterize the constitutive behavior of the material. We investigate the material response of commercial PVC foams with different densities, namely 130, 200 and 250 kg/m<sup>3</sup>, provided by the company Diab<sup>®</sup> and here indicated with their commercial name: Divinycell<sup>®</sup> HP130, HP200 and HP250, respectively. These densities are selected to have foams with a high mechanical response and suitable for high-end applications, as the mechanical properties increase with foam density.

The tests were conducted in a wide range of nominal strain rate, i.e. 10<sup>-3</sup>, 10<sup>-1</sup>, 10<sup>1</sup> and 10<sup>3</sup> s<sup>-1</sup>. All PVC foam samples have a nominal 12 mm × 12 mm square cross-section. The length of the samples was 15 mm for the tests at 10<sup>-3</sup> and 10<sup>-1</sup> s<sup>-1</sup>, while it was 10 mm for the ones tested at 10<sup>1</sup> and 10<sup>3</sup> s<sup>-1</sup>; samples with different lengths were adopted to match the strain rate over the prescribed range according to our testing facilities. Figure 1 shows an example of a PVC foam sample before and after compression; the black arrow marks the growth direction of the foam.

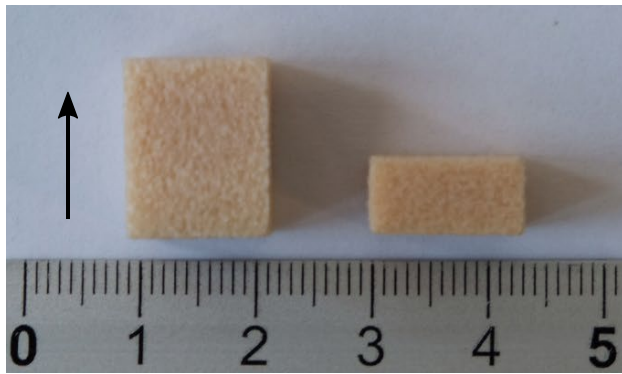


**Fig. 1** Example of HP130 PVC foam samples before and after compression test at  $10^{-3} \text{ s}^{-1}$

All samples were tested in compression, with the load acting parallel to the growth (out-of-plane) direction. To get a perception of the PVC foam's mechanical response according to the material orientation, we performed exploratory tests at different directions, observing a limited anisotropy as detailed in [34, 35]; however, for the purposes of this work, anisotropy does not play a relevant role and will not be considered. Three repetitions were carried out for each test condition, obtaining a strong repeatability of results; hence, only one curve for each test condition will be shown hereinafter. In addition, as expected for this class of material, a negligible lateral expansion was observed during compression tests, as depicted in Fig. 2 in the case of dynamic tests on the HP200 foam. The same behavior can be found for all the investigated foam densities, as captured by the movies reported in supplementary data provided along with the paper.

### Low and Medium Strain-rate Test Equipment

A pneumatic testing machine, model Siplan<sup>®</sup> equipped with a 3 kN load cell (Fig. 3 Servo-pneumatic testing machine), has been used to carry out the compression tests at strain rates from  $10^{-3}$  to  $10^1 \text{ s}^{-1}$ . The machine piston can reach a speed of 100 mm/s. The sampling rate for piston position and load was set to have approximately 1000 points at a nominal strain of 70%. The tested samples were obtained from PVC planks of three different densities, i.e. 130, 200 and  $250 \text{ kg/m}^3$ , corresponding to 0.09, 0.14, and 0.18 relative density, respectively.

In the low strain rate regime tests, i.e.  $10^{-3}$  and  $10^{-1} \text{ s}^{-1}$ , the piston was gently moved downwards, approaching the upper sample surface, and the test started when the preload reached the value of 2 N.

In the tests at medium strain rate (i.e.  $10^1 \text{ s}^{-1}$ ), the piston was moved to the uppermost position and accelerated from 0 to 100 mm/s before going into contact with the sample. In this way, the samples were deformed at the most constant

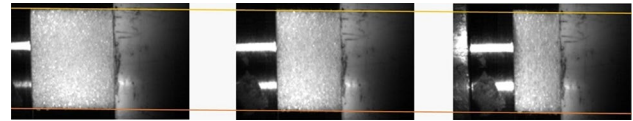


**Fig. 2** Snapshots of a HP200 PVC foam sample at three different instants during a dynamic test at  $10^3 \text{ s}^{-1}$ . The images highlight how the foam sample does not exhibit lateral expansion during the compression test

speed achievable with the used machine. The test was considered to start when the load exceeded 2 N. A perfect strain rate control cannot be achieved; however, the actual average strain rate was found to be in the range  $7.0 - 8.0 \text{ s}^{-1}$ , which was considered acceptable when compared to the target of  $10 \text{ s}^{-1}$ . Moreover, a small peak in the load cell measurement during the initial ramp was observed in all tests at  $10^1 \text{ s}^{-1}$ . This can be attributed to the problem of inertial effects and load oscillations which is well known in this kind of intermediate strain rate test [36], and dedicated machines have been developed to overcome the phenomenon [37]. Nevertheless, the oscillations in this case were very limited due to the intrinsic effect of material damping; in fact, even if no particular precautions were taken, the peaks were always less than 20% in amplitude of the plateau stress and were easily filtered out manually. An example of this manipulation is shown in Fig. 4.

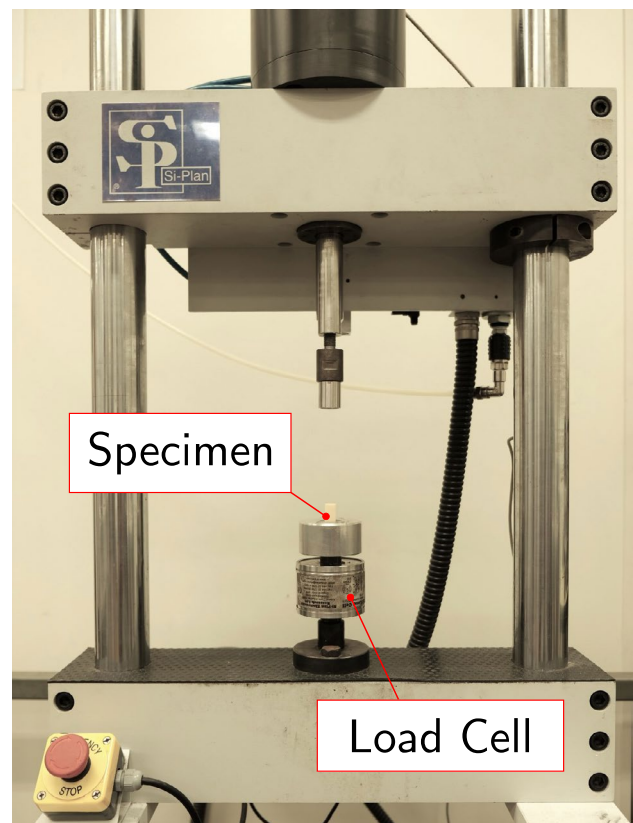


**Fig. 3** Servo-pneumatic testing machine

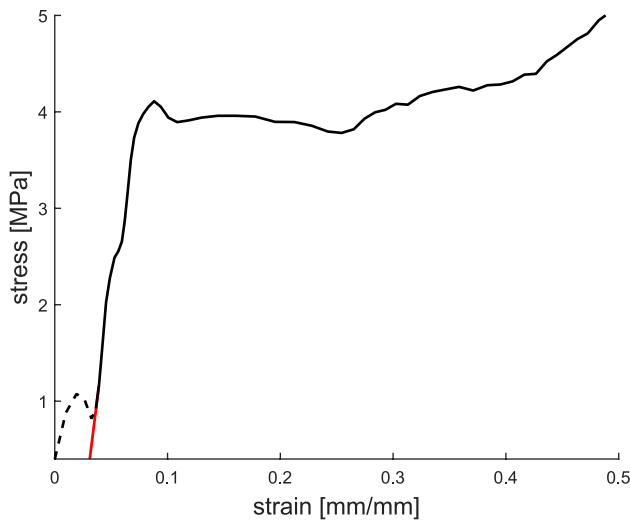


**Fig. 4** Example of manual peak removal in the loading ramp at  $10^1$   $s^{-1}$  due to inertia effect: the black dashed line indicates the initial peak observed experimentally, while the red straight line indicates the resulting correction

## High Strain-Rate Test Equipment

The dynamic tests were performed by means of the Split Hopkinson Pressure Bar (SHPB) shown in Fig. 5, whose calibration and adaptation to test soft materials are extensively described in [38–40].

The SHPB apparatus is made up of three aligned bars named pre-stressed, input and output bars, which are 3.0, 7.5 and 4.0 m long, respectively. All bars have a diameter of 18 mm. A compression wave is produced inducing a sudden release of the elastic energy stored in the pre-stressed bar, which is statically pre-loaded by means of an electro-mechanical actuator. This input wave travels through the input bar at the sound speed of the bar material and reaches the sample that is placed between the input and the output bars. While the sample is quickly deformed, the wave is partially transmitted to the output bar and partially reflected into the input bar. The strain induced by the incident  $\varepsilon_I(t)$ , reflected  $\varepsilon_R(t)$  and transmitted  $\varepsilon_T(t)$  waves, respectively, is measured by strain gauge rosettes placed on the input (subscript I) and output (subscript O) bars in full Wheatstone bridge configuration. The signals obtained are used to compute the load at the

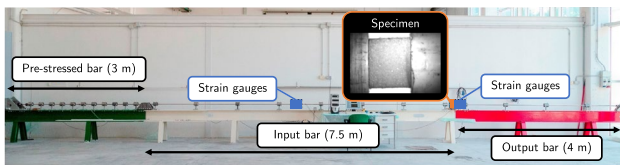


**Fig. 5** Split Hopkinson Pressure Bar setup

two edges of the sample that are in contact with the input and output bars, according to the equations:

$$P_I(t) = E_I \cdot A_I [\varepsilon_I(t) + \varepsilon_R(t)] \quad (1)$$

$$P_O(t) = E_O \cdot A_O [\varepsilon_T(t)] \quad (2)$$

where  $E$  is the elastic modulus and  $A$  the cross-section area of the bars,  $P_I$  and  $P_O$  are the loads on the sample computed at the input and output bar interfaces, respectively. Once the loads are calculated, the stresses can be determined by dividing the load values obtained by the sample cross-section area. The velocity  $\dot{u}$  at the two edges of the sample can be computed through the following equations:

$$\dot{u}_I(t) = C_I [\varepsilon_I(t) - \varepsilon_R(t)] \quad (3)$$

$$\dot{u}_O(t) = C_O [\varepsilon_T(t)] \quad (4)$$

where  $C$  is the sound speed of the bar material. The integration of equations (3) and (4) allows to calculate the engineering strain  $e$  experienced by the material according to equation (5), where  $L_s$  is the sample length:

$$e(t) = \frac{1}{L_s} \int_0^t [\dot{u}_I(t) - \dot{u}_O(t)] dt \quad (5)$$

The pre-stressed and input bars are made of aluminum (AA7075 T6) whereas, polyethylene terephthalate (PET) has been used for the output bar with the aim of increasing the sensitivity in the load measurement. To account for the viscoelastic nature of PET, the dedicated calibration and procedure shown in [41, 42] was exploited to post-process the experimental data. Tests were carried out on parallelepiped samples with a gauge length of 10 mm and a square section of 12 mm of side.

## Puncture Impact Test Equipment

The puncture impact tests were performed on square samples with 100 mm of side and 15 mm of thickness (Fig. 6(d)) in a drop weight tower Instron/Ceast<sup>®</sup> 9340 (Fig. 6(a)) equipped with the Data Acquisition System DAS 64 K by Ceast<sup>®</sup>. The latter allows to record material reaction force during the impact and to measure impactor initial velocity by means of an optical sensor placed just above the impacted area. From the force record, it is possible to extrapolate velocity, displacement and energy records through an integration process performed directly by the data system. Samples are placed onto a hollow circular base support with an inner diameter of 40 mm and are clamped by a pneumatic system, as shown in Fig. 6(c). The impactor used is shown in Fig. 6(b) and is characterized by a hemispherical shape, a diameter of 12.7



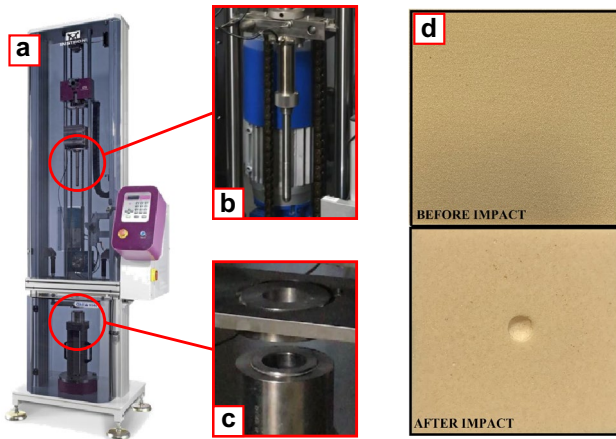


**Fig. 6** Puncture impact testing with Drop Tower machine (a), with details on the hemispherical impactor (b) and circular base support (c). An example of square sample before and after impact is shown in (d)

mm and an overall mass of 3.055 kg. PVC foam samples were tested at 1, 2.5, 5, 10 and 15 J, corresponding to an impact speed of 0.79, 1.27, 1.80, 2.55 and 3.11 m/s, respectively, which are included in typical range of impact speeds described in the standard ASTM D3763. Increasing impact energies and velocities were achieved by increasing the initial height of the impactor. The samples' perforation was detected at 2.55 m/s for HP130 and 3.11 m/s for HP200.

The impacted samples were subjected to a post-impact profilometric analysis to measure the residual indentation depth caused by the impactor. This non-destructive analysis was carried out with a laser profilometer Taylor Hobson® 150 and the acquired images were processed with the software TalyMap® 3D. A typical indentation profile is represented in Fig. 7.

## Constitutive Material Modelling

Cellular solids models can be divided into two categories: phenomenological models and micro-mechanical models. The phenomenological models aim to give the best fit of the experimental mechanical behavior without a direct relationship with the physics of the phenomenon. On the contrary, the micro-mechanical models are based on the analysis of the deformation mechanisms of the micro-cell structure under loading.

One widely accepted work was presented by Rusch [22] where the relationship between engineering stress  $s$  and engineering strain  $e$  was expressed as:

$$s(e) = Ae^m + Be^n, \quad (6)$$

where the exponents  $1 < n < \infty$  and  $0 < m < 1$ , while  $A$  and  $B$  are material coefficients. Liu and Subhash [24] suggested

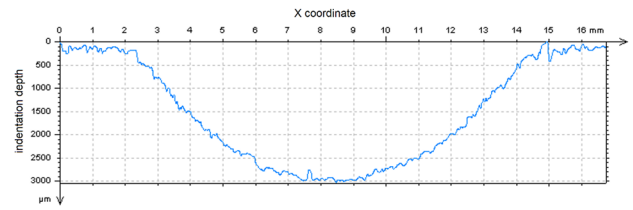


**Fig. 7** Indentation profile of an HP250 sample impacted at 5 J

a six parameters model to describe the quasi-static stress vs strain curve of polymeric foams:

$$s(e) = A \frac{\exp(\alpha e) - 1}{\exp(\beta e) + B} + \exp(c) [\exp(\gamma e) - 1], \quad (7)$$

Several non-linear constitutive laws have been proposed in the literature, from the seminal works of Rusch [22] to more recent model of Liu and Subhash [24], where the engineering stress  $s$  is expressed as a polynomial function of engineering strain  $e$ ; in this work, a further model proposed by Avalle et al. [25] has been adopted, with some modifications, to describe the non-linear stress-strain relationship. From the original five-parameter law [25]:

$$s(e) = A \left\{ 1 - \exp \left[ -\frac{E}{A} e (1 - e)^m \right] \right\} + B \left( \frac{e}{1 - e} \right)^n \quad (8)$$

the term  $m$  has been neglected since it was found to be unnecessary in the following model calibration; in addition, a term  $R$  was introduced at the denominator of the part related to the air response, as proposed in [22]. Hence, the final model is a modified five-parameters Avalle et al. model:

$$s(e) = A \left\{ 1 - \exp \left[ -\frac{E}{A} e \right] \right\} + B \left( \frac{e}{1 - e - R} \right)^n \quad (9)$$

The global uniaxial stress of the crushed foam is comprised of two parts. The former is governed by 2 coefficients  $E$  and  $A$ , which account in a simplified way for the solid material deformation and cell walls instability:  $E$  stands for Young's modulus,  $A$  is representative of the plateau stress. The second part of equation (9) is governed by coefficients  $B$ ,  $R$  and  $n$ , and accounts for the pressure increase of the air trapped in the closed-cell.  $B$  is a constant related to the initial air pressure,  $n$  is the polytropic coefficient of air (1.4 in adiabatic condition, 1.0 in isothermal condition) and in principle,  $R$  is the relative density or air volume fraction. This means that  $1 - R$  is the maximum achievable compressive strain when voids volume is reduced to zero and air pressure is infinite.

In this formulation, the model can represent reasonably well the loading characteristics of foams in quasi-static conditions. However, when dealing with polymer foams, the experience suggests that the material strength

is strongly influenced by strain rate, and the accumulated deformations are both plastic and elastic. A possible way to describe this behavior is to divide the model of the foam into two parts, one visco-elastic and the other visco-plastic. Berezvai and Kossa [33] adopted a two-layer model, where a classical Maxwell-type viscoelastic branch is placed in parallel with an elasto-plastic one. Both layers were specified using multi-linear isotropic elasticity. In this work, a similar scheme is used, as shown in Fig. 8, but the modified *Avallé* et al. model represented by equation (9) is used to describe the non-linear behavior of both layers as a function of strain.

In the model shown in Fig. 8, the arcs indicate that the springs are non-linear, their stiffness  $K$  given by the derivative of equation (9) with respect to strain:

$$K(e) = \frac{ds}{de} = E \exp\left(-\frac{E}{A}e\right) + Bn(1-R)e^{n-1}(1-e-R)^{-(n+1)} \quad (10)$$

The first spring in the second layer represents the initial elastic modulus, i.e. the stiffness  $E$  in equation (9); for stresses below the plateau stress  $A$ , the constitutive relation could be linearized, hence the arrow is dashed.

The second layer is made visco-plastic by including a multiplicative term which accounts for the sensitivity of the material to the strain rate  $\dot{e} = de/dt$  as described by Nagy et al. [27] and Jeong et al. [43]. While the works in [27, 43] use expressions of this term as function of both strain and strain rate, here we keep a formulation that depends only on  $\dot{e}$ , basically referring to the classical Johnson-Cook approach:

$$M(\dot{e}) = 1 + a \ln\left(\frac{\dot{e}}{\dot{e}_0}\right) \quad (11)$$

Hence, from the strain history, the stress in the visco-plastic branch is computed as:

$$s^{vp}(t) = \int_0^t K(e)M(\dot{e})\dot{e}dt \quad (12)$$

Moreover, the first layer is made visco-elastic by adding a dashpot in series to the non-linear spring, the stiffness of the visco-elastic layer is  $\alpha$  times the stiffness of the visco-plastic

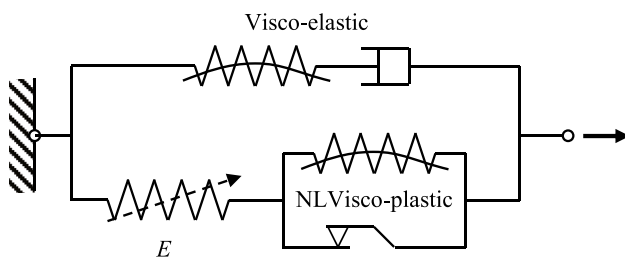


Fig. 8 Scheme of the 2-layer non-linear visco-elasto-plastic model

layer. This means that the stress in the visco-elastic branch at instant  $t$  is given by:

$$s^{ve}(t) = \exp\left(-\frac{dt}{\tau}\right)s^{ve}(t - \Delta t) + \alpha K(e)\exp\left(-\frac{dt}{2\tau}\right)\Delta e \quad (13)$$

where  $\Delta t$  and  $\Delta e$  are the increments in time and strain, respectively,  $\tau$  is a relaxation time, and  $\alpha$  is the ratio between the stiffness of the viscoelastic branch with respect to the total model stiffness. The total stress in the model is the sum of the visco-plastic and visco-elastic stresses:

$$s(t) = s^{vp}(t) + s^{ve}(t) \quad (14)$$

## Experimental Results and Model Calibration

The engineering stress and strain obtained from the experimental tests are reported in Fig. 9 in black dot curves. The data have been used within a procedure in Matlab<sup>®</sup> software, where the stress is analytically computed by applying the 2-layer model equations (13) and (14) to the measured strain histories. The *fmincon* built-in method was used to iteratively vary the coefficients of the model until the error function, defined as the root mean square of the difference between the experimental and numerical stress, was minimized. The analytical curves obtained by this fitting process are also shown in Fig. 9, where the different contributions to the global response are highlighted with different colors: the blue dashed lines represent the term given by equation (9), the green dashed lines represent the stress in the viscoelastic layer given by equation (13), the brown dashed lines represent the visco-plastic term given by equation (12), and the red lines represent the overall response of the model, that is the sum of the visco-plastic and visco-elastic responses as in equation (14).

The coefficients of best fit are reported in Table 1 together with the value of the error function. In the minimization process, the term  $n$  has been kept constant at 1.4, as it represents the adiabatic gas constant. It must be admitted that more solution sets could be achieved, providing similar good matching between experimental and analytical curves. In particular, the visco-elastic description could be improved by adding more Maxwell terms and/or performing relaxation/unloading tests. Nevertheless, all the achieved coefficients have a reasonable value if their physical meaning is considered: indeed, the coefficients  $A$  and  $E$  represent the plateau stress and the initial modulus, respectively, while  $B$  refers to the effect of the air trapped in the foam cells. These coefficients are seen to increase with foam density.  $a$  represents the strain-rate sensitivity of the visco-plastic response of the material when the strain-rate is higher than a threshold  $\dot{e}_0$ ;  $\alpha$  and  $\tau$  describe the contribution of the visco-elastic part to the global stiffness and the typical relaxation time, respectively.

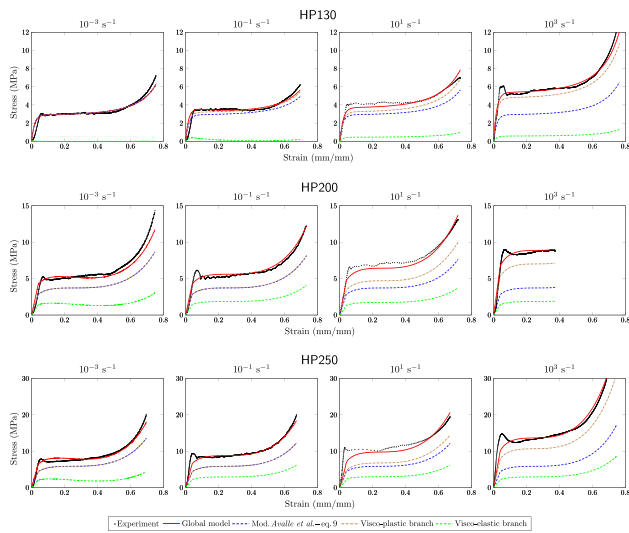


**Fig. 9** Stress-strain behavior at different strain rates for the three densities of PVC foams here investigated. The figures compare the experimental curves with the proposed visco-elasto-plastic modelling (i.e. the global model) and the quasi-static formulation introduced in equation (9). By considering each layer of the Maxwell model separately it is possible to disentangle the effects of the visco-elastic (Equation (13)) and visco-plastic (Equation (12)) branches, respectively

Finally, the energy absorption efficiency  $\eta$  can be computed according to [32]:

$$\eta(e) = \frac{1}{s(e)} \int_0^e s(e) de \quad (15)$$

The measured values for all three densities tested are plotted in Fig. 10: the efficiency slightly decreases with increasing density, moving from about 0.475 for HP130 to 0.425 for HP250. Moreover, the efficiency is slightly higher in the two fastest tests compared to the slowest ones. The densification or critical strain, that is the strain of maximum efficiency, appears to be quite stable with density, being in the range 0.5–0.6 for all tests.

### Finite Element Modelling

After material model calibration, the impact tests were simulated by means of the commercial Finite Element software. In particular, the Abaqus<sup>®</sup>/Explicit code was adopted because it is well suited for implementing user-defined

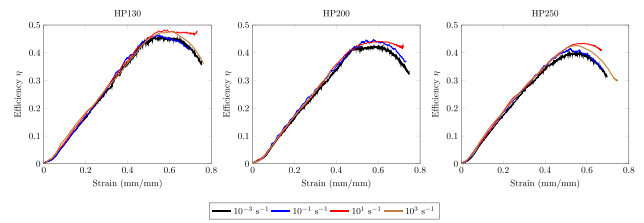


**Fig. 10** Evaluation of the energy absorption efficiency of foams at the three investigated densities according to different levels of strain rates achieved during the compression tests

constitutive models by means of user-defined Fortran sub-routines (VUMAT). All the numerical models in the following sections adopt the same explicit scheme for the stress reconstruction, here reported in detail in Appendix B. Basically, the numerical integration algorithm is based on the main assumptions of Von Mises yield surface, isotropic hardening and associative flow rule for the visco-plastic branch. Note that, in this paper, we kept the modelling of the plastic behavior relatively simple to be consistent with the data provided by the experiments above. Nonetheless, further experimental studies will be necessary to expand the constitutive modelling to include the anisotropic plastic behavior and understand the nature of the flow rule. It is also important to highlight that the integration scheme is mainly developed to handle the loading phase of the impact test and uses a damage variable to decouple the elastic strain from the plastic one; therefore, there is no formal involvement of the plastic flow rule equation in the strain decoupling. This aspect is also discussed in detail in the Appendix.

A 2D axisymmetric model of the PVC block impacted area and of the impactor has been built, as shown in Fig. 11(a). The PVC block is meshed with 2D axisymmetric reduced integration elements (CAX4R). Arbitrary Lagrangian-Eulerian (ALE) adaptivity option is used with some advantage in problem convergence. The impactor is discretized as a rigid surface, with a 3.055 kg mass and an initial velocity equal to the experimental values.

A mesh sensitivity analysis was performed, starting from a coarse mesh (1 × 1 mm) and refining up to the mesh shown in Fig. 11(a) (0.25 × 0.25 mm minimum element size), which was sufficient to stabilize the results in terms of residual rebound speed and max indentation depth within less than 1% variation. On the other hand, convergence issues have been experienced for higher impact energy and

**Table 1** Fitting coefficients of the two-layer visco-elasto-plastic model

	A [MPa]	B [MPa]	E [MPa]	m	n	a	$\dot{\epsilon}_0$ [s <sup>-1</sup> ]	$\alpha$	$\tau$ [s]	err %
HP130	2.86	0.48	178.8			0.0287	4.0e-4	0.485	0.0346	4.1%
HP200	4.98	1.20	228.0	0	1.40	0.0361	6.6e-2	0.389	0.056	3.5%
HP250	6.36	2.17	510.9			0.0320	1.0e-5	0.446	0.1	4.2%

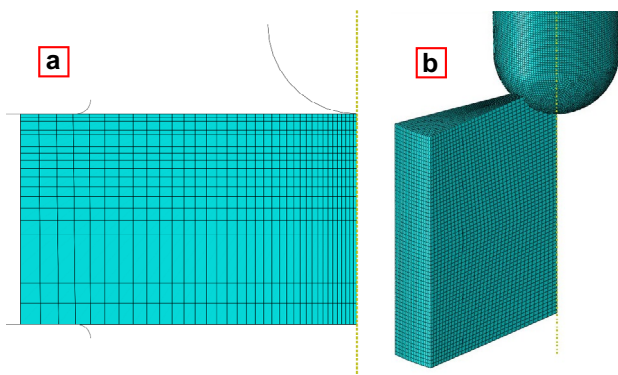


**Fig. 11** Finite element model of the impact tests

lower material density. Indeed, when the impact velocity is high and the material is soft, a very large deformation occurs suddenly in the elements that are in contact with the impactor; the material of these elements is likely to reach the plateau region of the stress-strain curve while the surrounding elements are much stiffer. The distortion of the softer elements determines the non-convergence of the explicit solver.

Hence, a second approach is used for modelling the impact test at higher speed and lower material density, which consists of a 3D Coupled Eulerian-Lagrangian (CEL) model, where a 15° sector of the PVC cylinder and steel punch have been reproduced. The model mesh is shown in Fig. 11(b). The normal displacements of lateral faces are constrained to reproduce a cyclic sector of the entire object and significantly reduce the computational cost. In such a simulation, the external Eulerian domain shown in blue is meshed with 3D reduced integration elements (EC3D8R). At the beginning of the simulation, only the elements that are inside the volume highlighted in red are filled with the solid material; then, the material can deform and move from its initial position into elements of the external Eulerian domain that are initially empty. In this model, the PVC block is fixed at its outer radius (i.e. the contacts with the tools have not been simulated), while its upper face is in contact with the impactor. The latter is discretized as a rigid surface, meshed with Lagrangian shell elements, and it was assigned a mass of 15/360·3.055 kg and an initial velocity equal to the experimental values.

Table 2 summarizes the approach used for all the simulations carried out. For the HP250 foam, only the simulation of the higher tested impact velocity, i.e. 3.11 m/s, which required the CEL approach. The HP200 foam's simulations required to switch to the Eulerian approach already at 1.8 m/s. For the HP130 foam, the standard Lagrangian approach failed to converge even at the slower speed, i.e. 0.79 m/s; hence, all HP130 simulations were performed with the 3D CEL method.

Stable time increment was in the order of 2E-8 s and 2E-9 s for the 2D axisymmetric and 3D Eulerian models, respectively.

The PVC foam surface is characterized by a relevant roughness; hence friction is expected to be high. A simple test with an inclined plane showed a friction coefficient at least as high as 0.45; a value of 0.7–0.75 was found in many case-studies [6] where polymeric foams are in contact with metallic, even smooth, plates. For this reason, “rough” behavior was chosen as the tangential contact behavior between the PVC and the tools.

As anticipated in the “Puncture Impact Test Equipment” section, perforation of the sample occurred in two experiments. A detailed simulation of this phenomenon involving material failure would have required a dedicated test campaign, with related damage and damage evolution models calibration, which were beyond the scope of the present work. For this reason, a simple damage criterion inspired by the Drucker-Prager model was implemented in the VUMAT code, which consists of deleting the elements whose shear stress exceeds a pressure-dependent threshold:  $\tau > \alpha + \beta p$ ;  $\alpha$  and  $\beta$  are density-dependent parameters that have been iteratively adjusted; their estimated values are  $\alpha = 6.0$  MPa and  $\beta = 1.0$  for HP130, and are  $\alpha = 6.5$  MPa and  $\beta = 1.2$  for HP200.

## Impact Tests Verification

### Finite Element Simulations' Results

The impact tests performed experimentally with the equipment described in the “Puncture Impact Test Equipment” section have been replicated numerically by means of the FE model and material subroutine VUMAT described in the “Finite Element Modelling” section. The results of the finite

**Table 2** Finite Element approaches used for impact tests simulations

Energy [J]	Speed [mm/s]	HP130	HP200	HP250
1	790	Eulerian 3D	Lagrangian Axisym	Lagrangian Axisym
2.5	1270	Eulerian 3D	Lagrangian Axisym	Lagrangian Axisym
5	1800	Eulerian 3D	Eulerian 3D	Lagrangian Axisym
10	2550	Eulerian 3D	Eulerian 3D	Lagrangian Axisym
15	3110	-	Eulerian 3D	Eulerian 3D



element simulations are reported in the following figures, in terms of equivalent strain  $\epsilon_e$  at the instant of maximum penetration depth of the impactor (Fig. 12) and after the impactor rebound (Fig. 13).

Figure 12 shows that the equivalent strain can be as high as 1.5 (corresponding to about 0.8 of compressive engineering strain). As expected, the equivalent strain increases with impactor speed and decreases with foam density. By observing the deformed profile, it is also evident that the indentation depth increases with impact energy and decreases with the foam density. It is worth noting that high equivalent strain is achieved, as expected, in the central part of the PVC block, which is the region that goes first into contact with the impactor.

However, as the penetration increases, the location of the maximum equivalent strain moves away from the center of the contact region, toward the outer region of contact with the impactor. It is from this outer location that PVC failure starts in the cases of complete perforation. Figure 13 shows the partial recovery of deformation that occurs when the impactor rebounds. It can be observed that the indentation left by the impactor is less pronounced with respect to Fig. 12, and the equivalent strain reduces, meaning that part of the deformation was stored elastically. Hence, the contour maps here shown can be regarded as distributions

of the equivalent plastic strain. Note that for the impacts of HP130 at 10 J and HP200 at 15 J, where sample perforation occurred, the pictures in Fig. 12 refer to the last instant before damage initiation (first element deletion), while the pictures in Fig. 13 refer to the last simulated time step, where the impactor displacement exceeds the sample thickness.

### Results Comparison

The charts reported in Figs. 14 and 15 compare the results of the FE simulation with the experimental measurements, in terms of impactor speed and displacement. Figure 14 exhibits that the calibrated constitutive model and its implementation into the FE code can provide a very good description of the PVC block behavior, as the impactor deceleration is very well reproduced, especially at high-medium speed. A slightly less accurate prediction is observed when the impactor speed becomes close to zero or inverts its sign, during the rebound.

Note that for the impacts of HP130 at 10 J and HP200 at 15 J, the FE curves in red are dashed after the damage initiation; the divergence from experimental curves occurs since damaged elements are instantaneously deleted, without any damage evolution or stress softening.

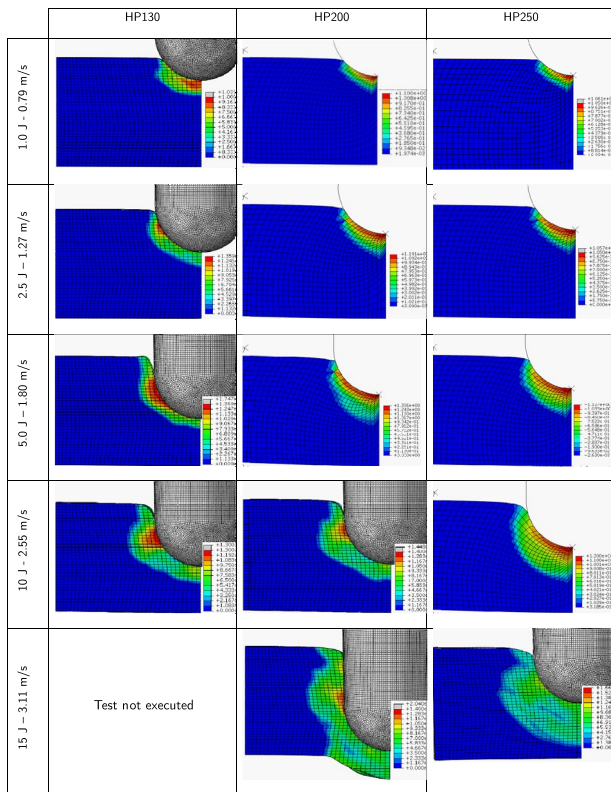


Fig. 12 Contour maps of equivalent strain from FE simulations of impact tests at the instant of maximum penetration

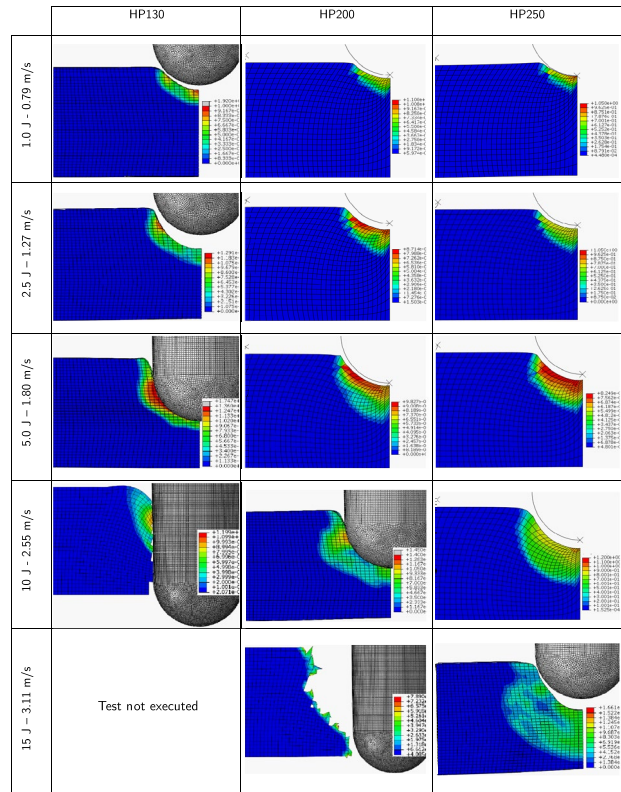


Fig. 13 Contour maps of equivalent strain from FE simulation of impact tests after rebound

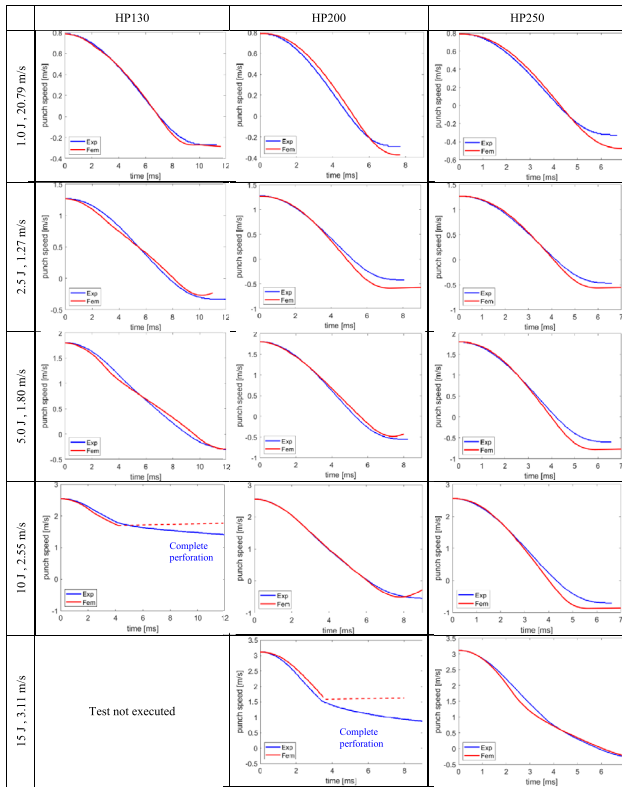


Fig. 14 Experimental vs. Numerical impactor speed

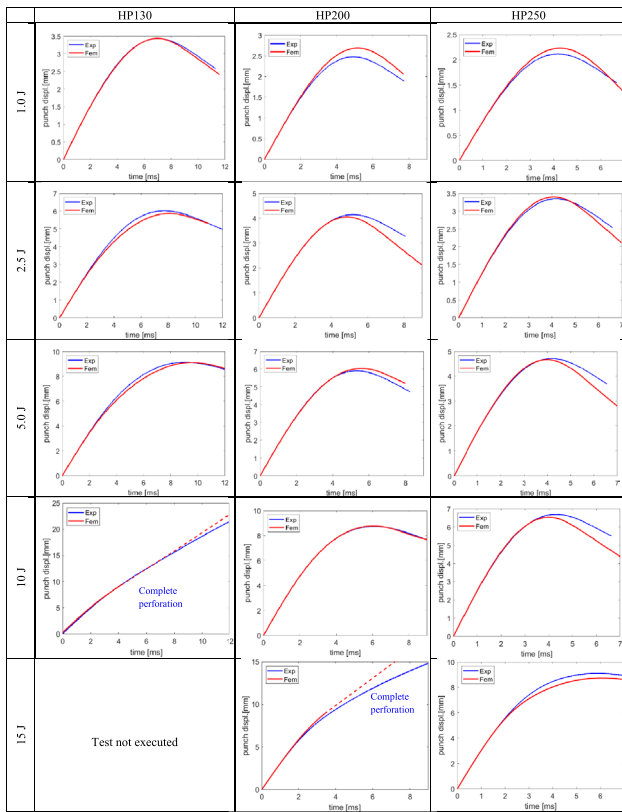


Fig. 15 Experimental vs. Numerical impactor displacement

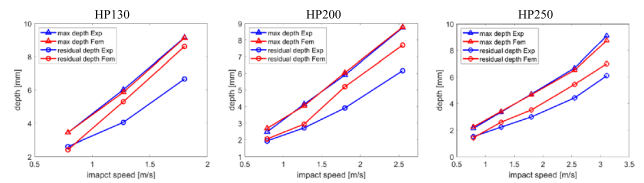


Fig. 16 Experimental vs numerical indentation depth

Looking at the impactor displacement histories in Fig. 15, a similar matching between experimental and numerical curves can be detected, and, in some cases, the FE simulations predict a slightly higher rebound of the impactor. The displacement is considered to start from the instant of first contact of the impactor with the PVC block and is reported as a positive value that coincides with the indentation depth except for the slight deflection of the PVC block.

By subtracting the deflection of the PVC block from the displacement, the net depth of the indentation is obtained. Figure 16 reports the net indentation depth as a function of impact speed for the three different PVC densities here considered. Note that the tests at 2.55 m/s on HP130 and at 3.11 m/s on HP200 are not shown since complete perforation was achieved. The lines with triangular markers refer to the max hole depth achieved during the tests, as measured by experimental equipment (in blue) and by FE analyses (in red). The matching is very good in all cases. The lines with circular markers refer to the residual indentation depth. It must be highlighted that the residual depth was measured experimentally, by means of a profilometer, hours after the tests, whereas the numerical results refer to the last instant of the simulation (which is in the order of milliseconds after the impactor rebound). Hence, further stress relaxation and strain recovery could be expected, thus explaining the overestimation of the residual indentation depth predicted by FE observed in some cases.

## Conclusions

In this work, compression tests on PVC foams with different densities, namely 130, 200 and 250 kg/m<sup>3</sup>, have been carried out at different strain rates, nominally from 10<sup>-3</sup> to 10<sup>3</sup> s<sup>-1</sup>. The tests were conducted by means of a servopneumatic machine, exception made for the high-strain rate tests performed by using a Split Hopkinson Pressure Bar, used to infer the stress-strain curves of the material and the consequent energy absorption efficiency, which is above 0.4 for all tests. Slight increments in efficiency are observed for increasing strain rate or decreasing density.

Moreover, the stress-strain curves are used to calibrate a visco-elasto-plastic model based on a two-layer scheme. The minimization of an error function between the experimental and the analytical curves provides a reasonable estimation of parameters, to which a precise physical meaning can be attributed.

Once validated, the analytical model is exploited to simulate the impact response of the foams under study. In particular, the material analytical model is implemented in a commercial Finite Element solver. The comparison of the experimental and numerical results confirms the validity of the proposed model showing a good fitting of the curves. The main discrepancies between experimental and numerical data are observed in the residual indentation depth, but these differences can be explained considering that the experimental data were obtained through a profilometric analysis several hours after impact, whereas the FE simulation refers to the permanent indentation just after impactor rebound. This means that further stress relaxation and strain recovery phenomena intervene in the experimental case.

## Appendix A: Kinematics

The integration of stresses relies on their relationship with strains, expressed by the constitutive equations, and on the kinematics, which establish the link between strains and displacements at each material point. Moreover, in finite deformation problems where the material exhibits a strain rate dependency, the stress is controlled by the loading history and its calculation generally requires the formulation of the constitutive equations in rate form [44–46].

Let us consider a general material point P, whose position in the Euclidian space in the reference (undeformed) configuration at time  $t$  is mapped by the vector  $\mathbf{X}$ . At  $t + \Delta t$ , a load is applied to the material, which experiences a combination of rigid body translations, rigid body rotations and stretch; here, the updated position of P in the current (deformed) configuration is identified by the vector  $\mathbf{x}$ , so that  $\mathbf{x} = \mathbf{x}(\mathbf{X}, t)$ . Therefore, the deformation gradient tensor is defined as:

$$\mathbf{F} = \frac{\partial \mathbf{x}}{\partial \mathbf{X}}. \quad (16)$$

The deformation gradient  $\mathbf{F}$  can be uniquely decomposed into the product between a rotation tensor and a pure deformation (namely the stretch) tensor according to the polar decomposition theorem, viz.:

$$\mathbf{F} = \mathbf{R}\mathbf{U} = \mathbf{V}\mathbf{R}, \quad (17)$$

where  $\mathbf{R}$  is the rotation tensor, while  $\mathbf{U}$  and  $\mathbf{V}$  are the right and left stretch tensor, respectively. By applying the time-derivative to the deformation gradient, it is possible to introduce the spatial velocity gradient  $\mathbf{L}$  from the material point velocity  $\mathbf{v}$ :

$$\mathbf{L} = \frac{\partial \mathbf{v}}{\partial \mathbf{x}} = \frac{\partial \mathbf{v}}{\partial \mathbf{X}} \frac{\partial \mathbf{X}}{\partial \mathbf{x}} = \dot{\mathbf{F}}\mathbf{F}^{-1}, \quad (18)$$

which can be alternatively written using the polar decomposition as  $\mathbf{L} = \dot{\mathbf{R}}\mathbf{R}^T + \mathbf{R}\dot{\mathbf{U}}\mathbf{U}^{-1}\mathbf{R}^T$ . In turn, the velocity gradient can be decomposed into symmetric and antisymmetric parts as follows:

$$\mathbf{L} = \frac{1}{2}(\mathbf{L} + \mathbf{L}^T) + \frac{1}{2}(\mathbf{L} - \mathbf{L}^T) = \mathbf{D} + \mathbf{W}, \quad (19)$$

allowing to disentangle the rate of deformation, expressed by the tensor  $\mathbf{D}$ , and the continuum spin  $\mathbf{W}$ .

In finite element implementations, the constitutive equations are generally defined in a co-rotational coordinate system, where the basis system rotates with the material. This makes the co-rotational Cauchy stress tensor  $\boldsymbol{\sigma}'$  *objective*, i.e. independent from rigid body rotations and based only on the constitutive response of the material. The objectivity property is also important for introducing a consistent measure of the stress rate since the rate of Cauchy stress tensor  $\dot{\boldsymbol{\sigma}}$  and the rate of deformation  $\mathbf{D}$  cannot be employed together. It is worth considering that the Cauchy stress  $\boldsymbol{\sigma}$  is expressed in the deformed configuration, which means that the application of only rigid body rotations makes  $\boldsymbol{\sigma}$  changing with time ( $\dot{\boldsymbol{\sigma}} \neq 0$ ) although the rate of deformation tensor  $\mathbf{D}$  is zero. Therefore, the stress rate should be defined following the so-called corotational derivative (also known as Lie Derivative), to provide a measure of the stress rate independent from rigid body rotations and based only on the constitutive behavior of the material:

$$\dot{\boldsymbol{\sigma}}_L = \dot{\boldsymbol{\sigma}} - \mathbf{L}\boldsymbol{\sigma} - \boldsymbol{\sigma}\mathbf{L}^T; \quad (20)$$

in particular, Abaqus<sup>®</sup>/Explicit uses a particular formulation of the Lie Derivative which considers only the first term of the velocity gradient  $\boldsymbol{\Omega} = \dot{\mathbf{R}}\mathbf{R}^T$  (called angular velocity tensor), namely the Green-Naghdi stress rate:

$$\dot{\boldsymbol{\sigma}}_{GN} = \dot{\boldsymbol{\sigma}} - \boldsymbol{\Omega}\boldsymbol{\sigma} + \boldsymbol{\sigma}\boldsymbol{\Omega}. \quad (21)$$

The use of a co-rotational coordinate system has also important implications on the definition of the strain increment employed for the stress calculation. Looking at equation (19), the rate of deformation can be written as:

$$\mathbf{D} = \frac{1}{2}\mathbf{R}(\dot{\mathbf{U}}\mathbf{U}^{-1} + \mathbf{U}^{-1}\dot{\mathbf{U}})\mathbf{R}^T = \mathbf{R}\mathbf{D}'\mathbf{R}^T, \quad (22)$$

where  $\mathbf{D}'$  indicates the rate of deformation before rigid body rotations, that is independent from the coordinate system (i.e. objective). The numerical integration of the constitutive equation in large strain problems often assumes that the principal directions of the right stretch tensor  $\mathbf{U}$  are kept constant during the deformation increment, so the principal material lines of  $\mathbf{U}$  and  $\dot{\mathbf{U}}$  are coincident at the end of the increment. Since the right stretch tensor  $\mathbf{U}$  and  $\dot{\mathbf{U}}$  are symmetric, the rotationless rate of deformation becomes:

$$\mathbf{D}' = \dot{\mathbf{U}}\mathbf{U}^{-1}, \quad (23)$$

where the product  $\dot{\mathbf{U}}\mathbf{U}^{-1}$  is also symmetric and makes the principal directions of  $\mathbf{D}'$  also aligned with the principal material lines of the right stretch tensor. Therefore, the strain increment  $\Delta\boldsymbol{\varepsilon}'$  can be defined by integrating  $\mathbf{D}'$  at the beginning and at the end of the increment:

$$\Delta\boldsymbol{\varepsilon}' = \int_t^{t+\Delta t} \mathbf{D}' d\tau = \ln \mathbf{U}|_t^{t+\Delta t}. \quad (24)$$

The  $\boldsymbol{\varepsilon}' = \ln \mathbf{U}$  is also known as logarithmic Hencky strain tensor, which is expressed as Lagrangian quantity in equation (24). And describes the deformation in the material coordinate system. Exploiting the objectivity property of  $\mathbf{D}'$ , it is straightforward to demonstrate that the  $\Delta\boldsymbol{\varepsilon}'$  corresponds to the strain increment provided by Abaqus<sup>®</sup>/Explicit in the co-rotational coordinate system. The use of the logarithmic strain increment is common in FE applications and has foundations in the incremental deformation theory based on the minimum plastic work path (proportional logarithmic strain path); further details about its formulation and implementation are reported in [47, 48] for the case of finite deformations in anisotropic plasticity problems.

## Appendix B: Explicit Integration Scheme in the VUMAT Subroutine

At each time increment, the integration of the constitutive equation associated with the modified Avalle et al. material model is performed according to the explicit algorithm summarized in Fig. 17; the integration scheme has been implemented in the Abaqus<sup>®</sup> commercial FE code through a VUMAT subroutine and is valid for both 2D axisymmetric and 3D Coupled Eulerian-Lagrangian numerical models presented in the “Finite Element Modelling” section.

Even if less important in energy absorption applications, the unloading phase has been considered in this work. The unloading from the maximum strain is modelled differently for the visco-elastic and visco-plastic branches, as shown in Fig. 18. When the load is removed, the first branch has a complete strain recovery, following the typical hysteretic loop observed in visco-elastic materials. This is mathematically achieved using equation (11) with negative strain increments. The second branch follows an elastic unloading, with slope equal to a damaged Young’s modulus  $E_d = E \cdot (1-D)$ ; thus a permanent deformation  $\varepsilon_p$  is predicted when the stress is removed. The damage variable  $D$  was considered here to coincide with the maximum compressive strain  $\varepsilon^*$  achieved during the loading phase.

Let us consider that all the mechanical quantities such as the total stress  $\boldsymbol{\sigma}$ , the stresses on the viscoelastic and viscoplastic branches  $\boldsymbol{\sigma}^{ve}$  and  $\boldsymbol{\sigma}^{vp}$ , the total strain  $\boldsymbol{\varepsilon}$  and

```

Input :  $\boldsymbol{\sigma}(t)$ ,  $\boldsymbol{\sigma}^{ve}(t)$ ,  $\boldsymbol{\sigma}^{vp}(t)$ ,  $\boldsymbol{\varepsilon}(t)$ ,  $\Delta\boldsymbol{\varepsilon}$ ,  $\boldsymbol{\varepsilon}(t)$ ,  $\boldsymbol{\varepsilon}^*$ ,  $t$ ,  $\Delta t$ 
Output:  $\boldsymbol{\sigma}(t + \Delta t)$ ,  $\boldsymbol{\sigma}^{ve}(t + \Delta t)$ ,  $\boldsymbol{\sigma}^{vp}(t + \Delta t)$ ,  $\boldsymbol{\varepsilon}(t + \Delta t)$ ,  $\boldsymbol{\varepsilon}(t + \Delta t)$ ,  $\boldsymbol{\varepsilon}^*$ 

Update strain quantities;
begin
    Total logarithmic strain:  $\boldsymbol{\varepsilon}_{ij}(t + \Delta t) = \boldsymbol{\varepsilon}_{ij}(t) + \Delta\boldsymbol{\varepsilon}_{ij}$ ;
    Von Mises equivalent strain:
     $\boldsymbol{\varepsilon}(t + \Delta t) = \frac{1}{\sqrt{2(1+\nu)}} \left\{ 3 \boldsymbol{\varepsilon}_{ij}(t + \Delta t) \boldsymbol{\varepsilon}_{ij}(t + \Delta t) - [\boldsymbol{\varepsilon}_{kk}(t + \Delta t)]^2 \right\}^{1/2}$ ;
    Strain rate:  $\dot{\boldsymbol{\varepsilon}}(t + \Delta t) = [\boldsymbol{\varepsilon}(t + \Delta t) - \boldsymbol{\varepsilon}(t)]/\Delta t$ ;
    Conversion to equivalent engineering strain:
     $e(t + \Delta t) = \exp(-\varepsilon_e) - 1$ ;
    Store maximum engineering strain:
    if  $\boldsymbol{\varepsilon}(t + \Delta t) > \boldsymbol{\varepsilon}^*$  then
        |  $\boldsymbol{\varepsilon}^* = \boldsymbol{\varepsilon}(t + \Delta t)$ ;
    end
end

Compute the stiffness  $K(e)$  (Eq. 12);
Convert the stiffness  $K(e)$  to true stiffness  $K(\boldsymbol{\varepsilon})$  (Eq. 26);
Compute the tangential stiffness matrix  $\mathbf{C}^{et}$ :
 $\mathbf{C}_{ijkl}^{et} = \frac{K(\boldsymbol{\varepsilon})}{2(1+\nu)} (\delta_{il}\delta_{jk} + \delta_{ik}\delta_{jl}) + \frac{K(\boldsymbol{\varepsilon})\nu}{(1+\nu)(1-2\nu)} \delta_{ij}\delta_{kl}$ ;

Stress calculation;
begin
    Update the stress on the viscoplastic layer:
    if  $\boldsymbol{\varepsilon}(t + \Delta t) \geq \boldsymbol{\varepsilon}(t)$  then /* Loading */
        Retrieve the stress increment:  $\Delta\boldsymbol{\sigma}_{ij} = \mathbf{C}_{ijkl}^{et} \Delta\boldsymbol{\varepsilon}_{kl}$ ;
         $\boldsymbol{\sigma}_{ij}^{vp}(t + \Delta t) = \boldsymbol{\sigma}_{ij}^{vp}(t) + M(\dot{\boldsymbol{\varepsilon}}) \Delta\boldsymbol{\sigma}_{ij}$ ;
    else /* Unloading */
        Compute the relaxation elasticity matrix  $\mathbf{C}^{ed}$  (Eq. 27);
         $\boldsymbol{\sigma}_{ij}^{vp}(t + \Delta t) = \boldsymbol{\sigma}_{ij}^{vp}(t) + \mathbf{C}_{ijkl}^{ed} \Delta\boldsymbol{\varepsilon}_{kl}$ ;
    end

    Update the stress on the viscoelastic layer:
     $\boldsymbol{\sigma}_{ij}^{ve}(t + \Delta t) = \exp(-dt/\tau) \boldsymbol{\sigma}_{ij}^{ve}(t) + \alpha K(\boldsymbol{\varepsilon}) \exp(-dt/2\tau) \Delta\boldsymbol{\varepsilon}_{ij}$ ;
    Total stress:  $\boldsymbol{\sigma}_{ij}(t + \Delta t) = \boldsymbol{\sigma}_{ij}^{ve}(t + \Delta t) + \boldsymbol{\sigma}_{ij}^{vp}(t + \Delta t)$ ;
end
    
```

Fig. 17 Explicit stress reconstruction scheme for PVC foams

the equivalent Von Mises strain  $\boldsymbol{\varepsilon}$  are known at the load step  $t$ ; the algorithm reconstructs the stress state for each integration point at  $t + \Delta t$  from the given strain increment  $\Delta\boldsymbol{\varepsilon}$ . As mentioned in the previous section, the integration of the constitutive equations is carried out according to the material co-rotational coordinate system (for the sake of clarity we omit the prime symbol to indicate co-rotational quantities), therefore, the Abaqus<sup>®</sup> solver rotates all the strain and stresses on the global coordinate system at the end of the increment to display the results.

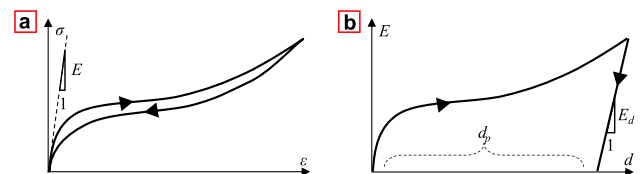


Fig. 18 Examples of the unloading mechanisms of the of the 2-layer non-linear visco-elasto-plastic model: **a** visco-elastic branch, **b** visco-plastic branch



As first stage of the stress reconstruction algorithm, the total strain field is updated to the current time increment and used to compute the equivalent Von Mises strain  $\epsilon(t + \Delta t)$ ; this equivalent measure of the strain is also exploited to determine the strain rate associated to the time increment  $\Delta t$ . Since the modified Avalle et al. model employed to describe the behavior of PVC foams is defined in terms of engineering stress and engineering strain quantities, the equivalent strain  $\epsilon$  is converted to the engineering strain  $e$ . The equivalent engineering strain is used for calculating the strain rate and the stiffness  $K$  according to equation (10). At this step, the stiffness  $K$  computed on the engineering curve is pulled back to the true (logarithmic)  $\sigma - \epsilon$  curve to have an expression of the tangential stiffness matrix  $\mathbf{C}^{et}$  consistent with the stress and strain measures used by the FE compiler. The compression tests reported in the “[Experimental Results and Model Calibration](#)” section have shown that the PVC foam is characterized by a Poisson’s ratio  $\nu$  equal to zero; in other words, the sample cross-section remains constant during the compression, so that the engineering stress  $s$  can be considered equal to the true stress  $\sigma$ . Considering the relationship between the engineering and true strains  $e = \exp(\epsilon) - 1$  the material stiffness according to the true curve is retrieved through:

$$K(\epsilon) = \frac{d\sigma}{d\epsilon} = \frac{ds}{de} = \frac{ds}{de} \frac{de}{d\epsilon} = K(e)\exp(\epsilon). \quad (25)$$

Before the stress integration, the algorithm also checks and stores the maximum amount of engineering strain  $\epsilon^*$  to compute the damaged elastic modulus in the case of unloading.

In the second stage, the stress is retrieved on the two Maxwell layers separately. The visco-plastic layer accounts for the inelastic behavior of the foam, which is mainly regulated by assigning a different material behavior between loading and unloading increments. Since the material is compressible and no locking occurs in the stress calculation, no plastic flow rule is needed and the material stiffness  $K(\epsilon)$  can be used directly to compute the stress increment  $\Delta\sigma^{vp}$ ; therefore, during the loading phase, the stress tensor is updated by using a multilinear isotropic elasticity framework where the stress increment is computed by multiplying the tangential stiffness matrix  $\mathbf{C}^{et}$  to the strain increment  $\Delta\boldsymbol{\epsilon}$ . This approach is valid for small-time increments indeed, meeting the requirements of the conditional stability in explicit solutions. On the other hand, when an unloading increment takes place, the stress  $\boldsymbol{\sigma}^{vp}(t + \Delta t)$  is obtained through the relaxation elasticity matrix  $\mathbf{C}^{ed}$  from the damaged Young’s Modulus  $E_d$ :

$$\mathbf{C}_{ijkl}^{ed} = \frac{E_d}{2(1 + \nu)} (\delta_{ij}\delta_{jk} + \delta_{ik}\delta_{jl}) + \frac{E_d\nu}{(1 + \nu)(1 - 2\nu)} \delta_{ij}\delta_{kl}, \quad (26)$$

where  $\delta_{ij}$  indicates the Kronecker delta.

Due to the multilinear elasticity framework and the assumption of small strain increments, the loading/unloading

criterion can be expressed through the comparison between the values of equivalent Von Mises strain at the current and the previous time step, as outlined by the *if*-loop in the stress update box in Fig. 17. Using the equivalent strain allows to tackle some of the difficulties of the common loading criteria defined in the stress space, as for differentiating the unloading from strain softening response of materials [49, 50], and offers a more general approach suitable for the proposed explicit integration algorithm.

Besides, the stress on the viscoelastic layer is reconstructed by means of equation (13); thus, the subroutine ends calculating the total stress for each integration point by combining the stress tensors from the viscoelastic and visco-plastic branches as in equation (14).

The implemented explicit integration scheme offers a straightforward implementation of the constitutive model, especially for the study of energy absorption applications, although it does not offer a generalized description of the whole material response mainly due to the following hypothesis on the visco-plastic branch:

- Unlikely the classical elasto-plasticity theory of metals and other works on PVC foams [26, 33, 51] where the total strain is additively decomposed into elastic and plastic parts, here the inelastic component of the strain tensor is expressed through damage [52]. The approach was already introduced in [53] for modelling the complex inelastic mechanisms of concrete related to the interaction between the plastic flow and the growth of microcracks in a heterogeneous material. In this paper, we used a simpler formulation for the damage function based on the maximum strain achieved during the loading phase; as consequence, the material can accumulate damage even in the case of very small strain increments, with no complete recovery of the initial shape.
- The algorithm does not decouple the elastic strain from the plastic strain at each  $\Delta t$ , but the total strain decomposition is performed only when the integration point experiences unloading increments.

It is also important to highlight that some of these assumptions are geared by the absence of direct experimental data on the PVC foams behavior under unloading conditions; therefore, as future developments, further experiments on cyclic loading-unloading tests should be performed to have a complete insight of the foam relaxation mechanisms.

**Supplementary Information** The online version contains supplementary material available at <https://doi.org/10.1007/s11340-023-00954-x>.

**Funding** Open access funding provided by Università Politecnica delle Marche within the CRUI-CARE Agreement. The authors have no relevant financial or non-financial interests to disclose. All authors certify that they have no affiliations with or involvement in any organization

or entity with any financial interest or non-financial interest in the subject matter or materials discussed in this manuscript. The authors have no financial or proprietary interests in any material discussed in this article.

**Data Availability** The datasets generated during and/or analyzed during the current study are available from the corresponding author upon reasonable request.

## Declarations

**Conflict of Interests** The authors have no competing interests to declare that are relevant to the content of this article.

**Open Access** This article is licensed under a Creative Commons Attribution 4.0 International License, which permits use, sharing, adaptation, distribution and reproduction in any medium or format, as long as you give appropriate credit to the original author(s) and the source, provide a link to the Creative Commons licence, and indicate if changes were made. The images or other third party material in this article are included in the article's Creative Commons licence, unless indicated otherwise in a credit line to the material. If material is not included in the article's Creative Commons licence and your intended use is not permitted by statutory regulation or exceeds the permitted use, you will need to obtain permission directly from the copyright holder. To view a copy of this licence, visit <http://creativecommons.org/licenses/by/4.0/>.

## References

- Ye N, Zhang W, Li D, Huang W, Xie W, Huang X, Jiang X (2017) Dynamic response and failure of sandwich plates with PVC foam core subjected to impulsive loading. *Int J Impact Eng* 109:121–130
- Balaban A, Tee K, Toygar M (2019) Low velocity impact behaviour of sandwich composite structures with E-glass/epoxy facesheets and PVC foam. *Procedia Struct Integr* 18:577–585
- Gupta N, Zeltmann S, Luong D, Doddamani M (2019) Core materials for marine sandwich structures. *Marine composite*. Woodhead Publishing, pp 187–224
- Zhou T, Cheng Y, Zhao Y, Zhang L, Wang H, Chena G, Liu J, Zhang P (2020) Experimental investigation on the performance of PVC foam core sandwich panels subjected to contact underwater explosion. *Compos Struct* 235:111796
- Aiello M, Corvaglia P, Hollaway L (2004) Experimental and numerical approach to buckling of laminated composite sandwich panel. *Advanced polymer composites for structural applications in construction*. Woodhead Publishing, pp 457–464
- Mills N (2007) Sport mat case study. *Polymer foams handbook*. Butterworth-Heinemann, pp 235–250
- Mostafa A, Shankar K, Morozov EV (2014) Experimental, theoretical and numerical investigation of the flexural behaviour of the composite sandwich panels with PVC foam core. *Appl Compos Mater* 21:661–675
- Tagarielli V, Fleck N, Deshpande V (2004) Collapse of clamped and simply supported composite sandwich beams in three-point bending. *Compos Part B Eng* 35:523–534
- Kulkarni N, Mahfuz H, Jeelani S, Carlsson L (2004) Fatigue failure mechanism and crack growth in foam core sandwich composites under flexural loading. *J Reinf Plast Compos* 23:83–94
- Imielińska K, Guillaumat L, Wojtyra R, Castaings M (2008) Effects of manufacturing and face/core bonding on impact damage in glass/polyester-PVC foam core sandwich panels. *Compos Part B Eng* 39:1034–1041
- Deshpande V, Fleck N (2001) Multi-axial yield behaviour of polymer foams. *Acta Mater* 49(10):1859–1866
- Colloca M, Dorogokupets G, Gupta N, Porfiri M (2012) Mechanical properties and failure mechanisms of closed-cell PVC foams. *Int J Crashworthiness* 17:327–336
- Lim G, Altstädt V (2009) Understanding the compressive behavior of linear and cross-linked poly(vinyl chloride) foams. *J Cell Plast* 45:419–439
- Wei Z, Nan Y (2016) High strain rate and quasi-static compression behavior and energy absorption characteristic of PVC foam. *Chall J Struct Mech* 2:212–215
- Chakravarty U, Mahfuz H, Saha M, Jeelani S (2003) Strain rate effects on sandwich core materials: an experimental and analytical investigation. *Acta Mater* 51:1469–1479
- Thomas T, Mahfuz H, Kanny K, Jeelani S (2004) High strain rate response of cross-linked and linear PVC cores. *J Reinf Plast Compos* 23:739–749
- Mines R (2007) Strain rate effects in crushable structural foams. *Appl Mech Mater* 7:231–236
- Tagarielli V, Deshpande V, Fleck N (2008) The high strain rate response of PVC foams and end-grain balsa wood. *Compos Part B Eng* 39:83–91
- Pal S, Maiti S, Subhash G (2010) Effect of microscopic deformation mechanisms on the dynamic response of soft cellular materials. *Mech Mater* 42:118–133
- Kidd TH, Zhuang S, Ravichandran G (2012) *In situ* mechanical characterization during deformation of PVC polymeric foams using ultrasonics and digital image correlation. *Mech Mat* 55:82–88
- Fox C, Kishore S, Senol K, Shukla A (2021) Experiments in measuring dynamic hydrostatic constitutive properties of soft materials. *Mech Mater* 160:103948
- Rusch K (1969) Load-compression behavior of flexible foams. *J Appl Polym Sci* 13:2297–2311
- Gibson L, Ashby M (1997) *Cellular solids*. Cambridge University Press, Structure and properties, Cambridge
- Liu Q, Subhash G (2004) A phenomenological constitutive model for foams under large deformations. *Polym Eng Sci* 44(3):463–473
- Avalle M, Belingardi G, Ibba A (2007) Mechanical models of cellular solids: parameters identification from experimental tests. *Int J Impact Eng* 34:3–27
- Gielen A (2008) A PVC-foam material model based on a thermodynamically elasto-plastic-damage framework exhibiting failure and crushing. *Int J Solids Struct* 45:1896–1917
- Nagy A, Ko W, Lindholm U (1974) Mechanical behavior of foamed materials under dynamic compression. *J Cell Plast* 10:127–134
- Faruque O, Liu N, Chou C (1997) Strain rate dependent foam - constitutive modeling and applications. *SAE Paper* 971076. <https://doi.org/10.4271/971076>
- Chou C, Zhao Y (1996) Development of foam models as applications to vehicle interior. *SAE paper* No. 952733. <https://doi.org/10.4271/952733>
- Zhang J, Kikuchi N, Li V, Yeess A, Nusholtz G (1998) Constitutive modeling of polymeric foam material subjected to dynamic crash loading. *Int J Impact Eng* 21(5):369–386
- Campana F, Mancini E, Pilone D, Sasso M (2016) Strain rate and density-dependent strength of AlSi7 alloy foams. *Mater Sci Eng A* 651:657–667
- Tan P, Reid S, Harrigna J, Zou Z, Li S (2005) Dynamic compressive strength properties of aluminium foams. Part i. *J Mech Phys Solids* 53:2174–2205
- Berezvai S, Kossa A (2017) Characterization of a thermoplastic foam material with the two-layer viscoplastic model. *Mater Today Proc* 4:5749–5754

34. Tita V, Caliri M Jr (2012) Numerical simulation of anisotropic polymeric foams. *Lat Am J Solids Struct* 9(2):259–279
35. Sergi C, Sarasini F, Tirillò J, Barbero E, Sanchez-Saez S, Sasso M, Mancini E (2021) Temperature, strain rate and anisotropy effects on compressive response of natural and synthetic cellular core materials. *Compos Struct* 260:113268
36. Sahraoui S, Lataillade J (1998) Analysis of load oscillations in instrumented impact testing. *Eng Fract Mech* 60:437–446
37. Bhujangrao T, Froustey C, Iriondo E, Veiga F, Darnis P, Mata F (2020) Review of intermediate strain rate testing devices. *Metals* 10(7):894
38. Martarelli M, Mancini E, Lonzi B, Sasso M (2018) Sensor calibration of polymeric Hopkinson bars for dynamic testing of soft materials. *Meas Sci Technol* 29:025601
39. Sasso M, Antonelli M, Mancini E, Radoni M, Amodio D (2017) Experimental and numerical characterization of a polymeric Hopkinson bar by DTMA. *Int J Impact Eng* 103:50–63
40. Sasso M, Mancini E, Chiappini G, Sarasini F, Tirillo J (2018) Application of DIC to static and dynamic testing of agglomerated cork material. *Exp Mech* 58(7):101–1033
41. Jeong K (2016) Constitutive modeling of polymeric foams having a four-parameter modulus function with strain rate sensitivity. *J Mech Sci Technol* 30(2):683–688
42. Rusch K (1969) Energy-absorbing characteristics of foamed polymers. *J Appl Polym Sci* 14:1133–1147
43. Jeong K, Cheon S, Munshi M (2012) A constitutive model for polyurethane foam with strain rate sensitivity. *J Mech Sci Technol* 26(7):2033–2038
44. Belytschko T, Kam W, Moran B (2000) *Nonlinear finite elements for continua and structures*. Wiley
45. Dunne F, Petrinic N (2006) *Introduction to computational plasticity*. OUP Oxford
46. Albrecht B (2008) *Elasticity and plasticity of large deformations*. Springer
47. Yoon J, Yang D, Chung K, Barlat F (1999) A general elasto-plastic Finite element formulation based on incremental deformation theory for planar anisotropy and its application to sheet metal forming. *Int J Plas* 15:35–67
48. Rossi M, Lattanzi A, Cortese L, Amodio D (2020) An approximated computational method for fast stress reconstruction in large strain plasticity. *Int J Numer Meth Eng* 121:3048–3065
49. Han DJ, Chen WF (1986) Strain-space plasticity formulation for hardening-softening materials with elastoplastic coupling. *Int J Solids Struct* 22:936–950
50. Chen WF, Yamaguchi E, Zhang H (1991) On the loading criteria in the theory of plasticity. *Comput Struct* 39:679–683
51. Berezvai S, Kossa A (2020) Performance of a parallel viscoelastic-viscoplastic model for a microcellular thermoplastic foam on wide temperature range. *Polym Test* 84:106395
52. Taher SE-DMF, Baluch MH, de Melo FJM (2002) Rational split of the strain tensor in elastoplastic damage mechanics. *J Strain Anal Eng Des* 37:117–124
53. Ortiz M (1985) A constitutive theory for the inelastic behavior of concrete. *Mech Mater* 4:67–93

**Publisher's Note** Springer Nature remains neutral with regard to jurisdictional claims in published maps and institutional affiliations.